Materials Research. 2025; 28: e20250479
DOI: https://doi.org/10.1590/1980-5373-MR-2025-0479

Enhanced Performance of $Al/Al_2O_3/CdSe/Bi_2O_3/Pt$ Structures Designed as High Conductance Channels, Negative Capacitance Sources and 5G/6G Technology Antennas

A. F. Qasrawi[a,b]* , *Samah Sameer Atari*[a]

[a]*Arab American University, Department of Physics, Jenin, Palestine.*
[b]*Istinye University, Department of Electrical and Electronics Engineering, 34010, Istanbul, Turkey.*

Received: May 31, 2025; Revised: August 20, 2025; Accepted: September 21, 2025

CdSe deposited onto Al/Al_2O_3 substrates and partially recoated with Bi_2O_3 nanosheets are designed as multifunctional electronic devices. The device contains two channels: one formed from Al/Al_2O_3/CdSe/Pt (ACP) and the other covered with an additional Bi_2O_3 layer (ACBP). Band diagram analyses of the channels indicate that the conduction bands of CdSe and Bi_2O_3 are well aligned. Additionally, structural investigations reveal enhanced crystallinity of CdSe on Al/Al_2O_3 substrates. Both ACP and ACBP channels exhibit resonance-antiresonance (RA) and negative capacitance (NC) effects in the microwave frequency domain. The presence of Bi_2O_3 nanosheets enhances the RA phenomena and increases the NC effect by more than eightfolds. While ACP channels display low conductance values, ACBP channels demonstrate enhanced conductance by 167 times at 1.26 GHz. Furthermore, when evaluated as microwave antennas in the frequency range of 0.009–6.0 GHz, ACBP channels show that Bi_2O_3 nanosheets enhance the power reflection of the antennas by more than three orders of magnitude. The antennas exhibit improved transmission and reflection coefficients, increasing from 86.4% to 99.5% and decreasing from 13.6% to 0.5%, respectively, at a carrier frequency of 3.10 GHz. The smart features of the devices make them promising candidates for advanced electronic applications, including 5G/6G technologies.

Keywords: *$CdSe/Bi_2O_3$, X-ray, negative capacitance effect, microwave antennas.*

1. Introduction

CdSe as a light sensitive dielectric material has captured wide interest owing to their applications in photonic and millimeter antenna technology. CdSe/CdS/ZnSe tri-layers designed as multiple core-shell nanopillar array structure designed to perform as a light-trapping efficient antenna for broad band photo-detection applications exhibited photo-responsivity of 0.43 A/W and external quantum efficiency of 0.98[1]. The features of these nanopillar arrays were mentioned promising for next-generation photodetectors applications[1]. CdSe/CdS and CdSe/CdS/ZnSe were also employed in the design of a room temperature terahertz camera. The design was based on the terahertz-visible photon up- conversion induced by charge transfer between luminescent quantum dots[2]. CdSe quantum dots are accounted as promising devices employable as dipole antenna arrays adequate for 5G/6G and terahertz technology[3].

Although CdSe based structures showed promising features in antenna and photo-detection technology, they suffer from humidity and poor electrical conductivity[4]. Low electrical conductivity in antenna technology causes more energy dissipation, high loses reducing their gain and poor impedance matching leading to increased voltage standing wave ratios and narrow bandwidths[5]. Literature data mentioned that interfacing CdSe with Al_2O_3 is an effective tool to fabricate CdSe quantum dots and thin film transistors[6]. CdSe quantum dots enabled enhanced photoluminescence in Al_2O_3[6]. Earlier works on this interface have shown their suitability for liquid crystal displays[7]. Because this kind of interfacing improved the performance of CdSe and Al_2O_3, they will be employed in this work to form a heterojunction device suitable for antenna and microwave technologies. These devices are important for mobile technology[8], integrated sensing and communication[9,10] and antenna arrays designed for defense technology[11,12]. In antenna technology attenuation of the dielectric permeability is necessary to control the cutoff frequency of the resonator. For this purpose Bi_2O_3 nanosheets are used to lower the dielectric loss in the designed cavity[13]. The nonmagnetic property of Bi_2O_3 caused much reduction in the permeability of the magnetodielectric Ni ferrite ceramics allowing for the fabrication of miniaturized antenna[14].

Based on the above infromation one possible approach to enhance the antenna performance and increase the electrical conductivity is to isolate the semiconducting layer from atmosphere by coating it with a conductive oxide layer having cations of lower ionic radius than that of Cd^{+2} so that broken bonds existing on the surface of CdSe is reacted and reduced[15]. One of these oxide layers is Bismuth oxide. Bi_2O_3 nanosheets of thicknesses of 100 nm which were deposited onto n-Si substrates increased the performance of Si antennas forcing excellent performance as quad band 5G/6G antennas[16]. The improved performance of Si antenna by Bi_2O_3 coating presented a motivation for designing a multifunction electronic device benefiting from the features of CdSe as dielectric material. The current devices are designed to perform as

*e-mail: atef.qasrawi@aaup.edu
Associate Editor: Jose Eiras.
Editor-in-Chief: Luiz Antonio Pessan.

negative capacitance sources, microwave resonators and high frequency antennas. The performance of the device which will be tested in the frequency domains of 0.01-1.80 GHz as negative capacitance and high conductance source, will also be evaluated as 5G/6G antennas in the carrier frequency domain of 0.009-6.0 GHz.

2. Experimental Details

Thin films of Al, CdSe and Bi_2O_3 are fabricated by the thermal evaporation technique under a vacuum pressure of ~10^{-5} mbar. All the source materials were ordered from Alpha Aesar firm and were of high purity (99.995%). The fabrication procedure was initiated by depositing Al films of thicknesses of (500 ± 11) nm onto ultrasonically cleaned glass substrates. Al films were then exposed to air for sufficiently long period (couple of weeks) of time to obtain Al_2O_3 layer onto its surface. The thickness of the Al_2O_3 layer was measured by interferometry techniques (Evolution 350 spectrophotometer equipped with PIKE VEE MAX-II refelctometer) which measured films of thickness of (140 ± 11) nm . The process is based on the difference between the thickness of the monitored film (500 ± 11) nm and the one determined by the interferometer (640 ± 11) nm. All films thicknesses were monitored during the evaporation cycles with the help of an Inficon- type STM-2 thickness monitor installed in the thermal evaporator (NORM-600). The correctness of the thicknesses was also confirmed by a profilometer (SOLID-IN II) capable of measuring down to 5.0 nm. CdSe layer thickness was (1000 ± 10) nm whilst Bi_2O_3 was (100 ± 5) nm. The top contacts were deposited onto the films by an ion coating of Pt targets of high purity (99.999%). A special mask designed antenna and waveguide arrays. The X-ray diffraction patterns were collected with a Rigaku Miniflex 600 XRD unit. The $p-$ and $n-$ types conductivities of CdSe and Bi_2O_3, respectively, were learned by the hot probe technique The impedance spectroscopy was measured using Agilent 4291B 0.01-1.80 GHz, equipped with 16453A dielectric material test fixture. The microwave reflection and transmission spectra were measured using ROHDE&SCHWARZ ZVL network analyzer 9k-6 GHz.

3. Results and Discussion

3.1. Design considerations

In this work we consider the design and fabrication of a class of microwave resonators used for high frequency applications. The device is composed of two stacked layers of *p*-CdSe (1.0 μm) and n-Bi_2O_3 (100 nm) deposited onto oxidized Al thin films (640 nm) and top contacted with platinum point contact of area of 0.0314 cm^2. Because both of the CdSe and Bi_2O_3 exhibited similar electron affinities ($q\chi$) of values of 4.95 eV[17,18] and 4.94 eV[19], respectively, the conduction bands of these two layers are well aligned resulting in free electron transport from one layer to another. No conduction band offset ($\Delta E_c = q\chi_{CdSe} - q\chi_{Bi2O3} \approx 0.0$ eV) existed between the two layers. However, because as measured in our laboratory by spectrophotometry techniques, the energy band gaps of CdSe and Bi_2O_3 are 1.97 eV and 3.52 eV, respectively, the valence band offset ($\Delta E_v = \Delta E_g - \Delta E_c$) is 1.55 eV. This value of valence band offset is large enough to result in single carrier transport and wide depletion region in the *n*-side[20]. On the other hand, at the Al_2O_3/CdSe interface, as the electron affinity of Al_2O_3 is 2.38 eV and the energy band gap is 6.65 eV[21], the conduction and valence band offsets are 2.57 eV and 2.11 eV, respectively. In addition, the work function of Al is 4.30 eV[22] and that of Al_2O_3 is 4.70 eV[23] leading to an ohmic nature of contact. Because the work function ($q\phi$) of n-Bi_2O_3 is 4.99 eV[24], at the Pt ($q\phi_{Pt}$=5.65 eV)/Bi_2O_3 a none ohmic (Schottky) nature of contact prevails at that interface. The hybrid structure made of Al/Al_2O_3/CdSe/Bi_2O_3/Pt (abbreviated as ACBP) exhibit large barrier height of $q\varphi = q\phi_{Pt} - q\chi_{Bi2O3} = 0.71$ eV at the Pt/Bi_2O_3 sides whilst no barrier exists at the Al/Al_2O_3 interface exists. The energy band diagram of the hybrid structure is shown in Figure 1.

The experimental design also included a channel composed of A/Al_2O_3/CdSe/Pt (abbreviated ACP). The property of this channel is the lack of Bi_2O_3 nanosheets and as $q\phi_{Pt} < q\phi_{p-CdSe}$, a Schottky arm is present. This channel will allow visualization of the role of Bi_2O_3 nanosheets on the performance of the device.

The working principle of this device is highly complex and affected by the Schottky barrier. It is mostly governed by thermionic emission at the Pt/Bi_2O_3 interface and by charge carrier diffusion at the $p-\text{CdSe}/n-Bi_2O_3$ interface. The back side of the device allows electron transport by tunneling due to the ohmic nature of contact. Under forward biasing conditions all device components contribute to the current follow. The relation between the values of the forward to the reverse currents are mainly identified by the effective barrier heights and donor/acceptor concentrations. Such features of devices are reported suitable for high-frequency, optoelectronic, or memory applications[20,22,24].

3.2. Device fabrication

The schematic and the optical images for the ACBP and ACP channels are presented as inset-1 and inset-2 of Figure 2, respectively. The three point contacts at each side represent three distinct channels of similar characteristics whilst the two bars are designed to perform as waveguides. The distance between the two bars is 2.0 mm. One millimeter is on ACBP and another one on the ACP channel. Figure 1 also show the X-ray diffraction (XRD) patterns for the samples under study. The Al substrate displayed peaks corresponding to cubic Al ($a = b = c = 4.04\,\text{Å}$, space group $Fm-3m$) and hexagonalAl_2O_3. The lattice parameters for this unit cell are $a = b = 4.844\,\text{Å}$, $c = 13.27\,\text{Å}$ and space group $R-3c$) (Crystallography Open Database (COD: 9007635)). Al_2O_3 is formed on the surface of Al because of the purposely exposure of the aluminum surface to ambient air for long period of time. In addition, the XRD patterns of Bi_2O_3 nanosheets which are shown in Figure 1, displayed no sharp peaks indicating the amorphous nature of the Bi_2O_3 nanosheets.

On the other hand, sharp patterns of CdSe coated onto glass (for comparison) and onto Al substrates indicated the crystalline nature of the grown films. Particularly, the CdSe films coated onto glass and onto Al/Al_2O_3 substrates exhibited polycrystalline nature. The sharp diffraction patterns corresponded to hexagonal CdSe of lattice parameters of $a = b = 4.30\,\text{Å}$,

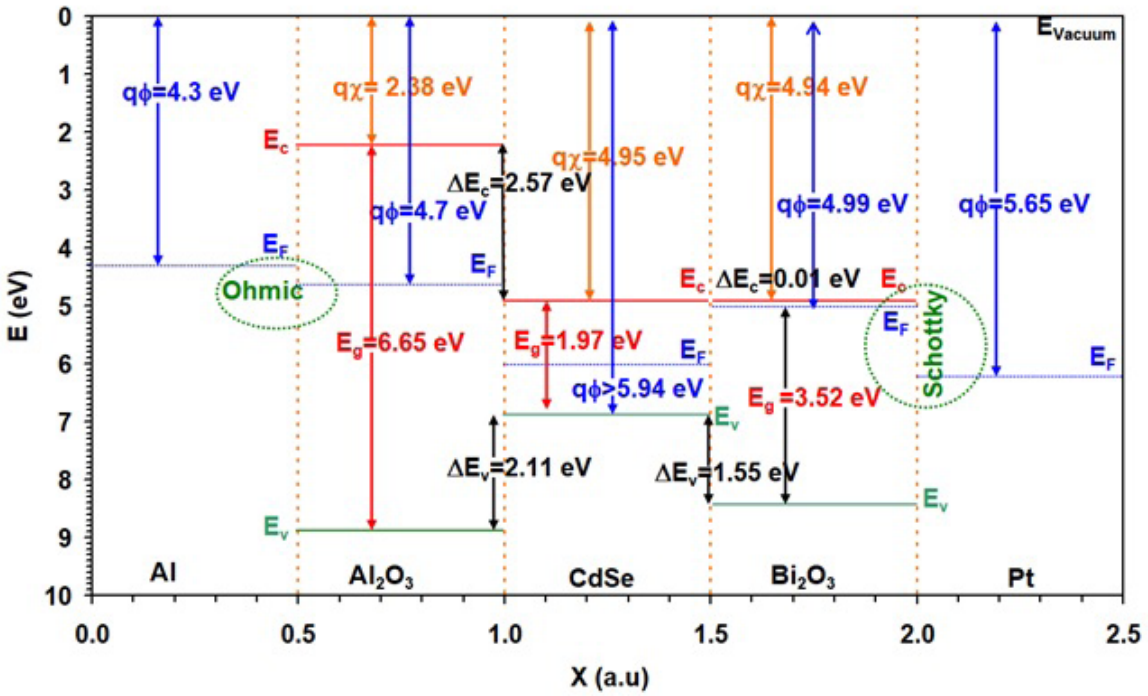

Figure 1. The energy band diagram for the Al/Al_2O_3/CdSe/Bi_2O_3/Pt devices.

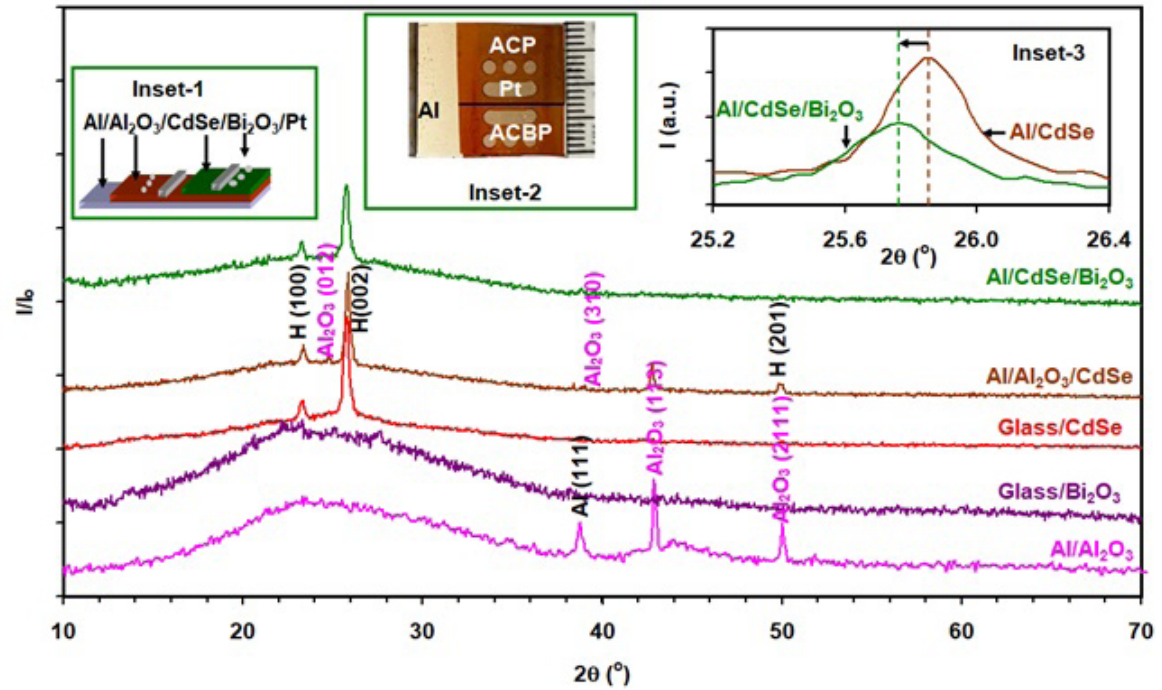

Figure 2. The X-ray diffraction patterns for the device layers. Inset-1, inset-2 and inset-3 showing the schematic, the optical image and the enlargement of the maximum peak, respectively.

$c = 7.02\,Å$, $P63mc$, (PDF card no: 00-002-0330). Depositing the films onto oxidized aluminum substrates showed the same structure with slight peak shifts and intensity variations resulting from Al/CdSe interactions. Actually as presented in Table 1, the sharpest peak observed at diffraction angle of $2\theta = 25.75^o$ shifted to $2\theta = 25.85^o$ and the intensity of the

peak increased by 9.4%). Determining the strain $\in = \frac{\beta}{4tan\theta}$[24], the crystallite size $D = 0.94\lambda/(\beta\cos(\theta)$[24], the stacking faults percentages $SF\% = \frac{2\pi^2\beta}{45\sqrt{3\tan(\theta)}}$[15], and the line defect density along the $c-$axis $\delta = \frac{15\,\varepsilon}{cD}$[24] from the maximum peak broadening at full wave half maximum (β), allowed gaining information about possible structural modifications. The structural parameters are listed in Table 1. As seen from the table Al substrates enhanced the crystallinity of CdSe by increasing the crystallite sizes from 26 nm to 32 nm, decreasing the strain by 19.2% and decreasing the stacking faults percentages from 0.30% to 0.25%. The line defects concentration also decreased by 34.2%. The latter result are worth of consideration because less defect concentration necessarily means improved carrier confinement within the active region of the device[25]. Such confinement increases the efficiency of electron transport, resulting in higher electron mobility and more effective device performance. In addition, the decreased strain values are mentioned playing a role in modifying the band alignment at hetero-interfaces, which in turn affects tunneling probabilities and barrier heights[25].

It is clear that Al/Al_2O_3 substrates induced the crystallinity of CdSe. Metal induced crystallization resulted from the diffusion of some of the Al^{+3} ions into the lattice of CdSe[26]. Because the ionic radius of Al^{+3} being 54 pm is less than that of Cd^{+2} (97 pm), Al^{+3} can fill vacant sites of Cd^{+2} inducing the crystallinity of CdSe by reducing the number of broken bonds[27]. The formation of a eutectic layer between CdSe and Al/Al_2O_3 substrates can also lead to the enhanced crystallinity of the CdSe layer[28]. The eutectic layers are formed because of bond length of Al-Se being 325 pm[29] is smaller than that of Cd-Se (262 pm[30]) which makes Se atoms having tendency to complete bonds with Al rather than Cd.

It can also be observed in Figure 1 that coating of Al/Al_2O_3/CdSe films with Bi_2O_3 nanosheets suppressed the sharp peaks of Al_2O_3 due to their weak reflections which became invisible with increased thicknesses of the stacked layers. The amorphous nature of Bi_2O_3 nanosheets strongly affect the observed XRD patterns. It can be seen from inset-3 of Figure 1 that the major peak of hexagonal CdSe is shifted toward lower diffraction angles and the intensity of the peak decreased (Table 1). The peak of ACBP films is broader. The shift in the major peak is ascribed to the lattice expansion of (002) planes caused by ionic substitutions and enhancement of lattice distortions[31]. The calculated structural parameters of these films are also presented in Table 1. The table shows that the crystallite size decreased from 32 nm to 25 nm, the microstrain, stacking faults and defect concentration remarkably increased. Numerically, the defect concentration increased from 3.46×10^{11} lines/cm^2 to 6.34×10^{11} lines/cm^2 upon coating Al/Al_2O_3/CdSe films with Bi_2O_3 nanosheets. The increase in the defect concentration reaches 83.23%. The decreased crystallite sizes and increased microstrain and stacking faults percentage results from amorphization that starts from the amorphous surface of the stacked layers[32]. The higher dislocation density (Table 1) and high strain resulting from interstitial substation of some Bi^{+3} (103 pm) ions in the lattice of CdSe also accounts for the decreased crystallite sizes[33].

The surface roughness measurements which were held on the samples using a profilometer have shown that Al/Al_2O_3 and CdSe films exhibited average surface roughness (R_a) values of 47 nm and of 13 nm, respectively. Bi_2O_3 nanosheets displayed R_a values of 11 nm. Coating CdSe films with Bi_2O_3 increased the average surface roughness to 25 nm. Literature data mentioned that increased roughness may result in signal attenuation at high frequencies[34]. The structural and surface roughness investigations ended with the result that ACP channel is of enhanced crystallinity, reduced roughness, decreased defect concentration and narrower crystallite boundaries owed to increased crystallite sizes. The ACBP channel exhibited higher roughness values, weaker crystallinity, larger crystallite boundaries and larger defect concentrations.

3.3. Negative capacitance and high conductance sources

To explore the possible applications of the device under study, the ACBP and ACP channels were sequentially imposed between the terminals of an impedance (Z) analyzer connected to material/dielectric fixture. An ac signal of low amplitude (V_o ~ 0.01 V) of wave forms and varying frequency in the frequency (f) domain of 0.01-1.80 GHz was applied. The propagating signal is of the form, $\tilde{V} = V_o e^{\pm i\omega t}$ with $\omega = 2\pi f$ being the radial frequency. The measured admittance ($Y = 1/Z$) allows determining the capacitance (C) of the device through the relation[35],

$$C = \frac{\varepsilon_r A}{d} = \frac{Y}{i\omega\varepsilon_o} \quad (1)$$

Here, ε_r is the relative dielectric constant, A is the electrode and d is the thickness of the device. The capacitance spectra are illustrated in Figure 3a. It is clear from the figure that the capacitance exhibit interesting features illustrated by the resonance and antiresonance (RA) effects in addition to the negative capacitance (NC) effect. The capacitance values and RA peaks positions are highly influenced by the Bi_2O_3 coating. The ACBP channel displayed larger capacitance values as compared to the capacitance of ACP channel which lacks of the second oxide layer. While ACP channels exhibited resonance at 1.37 GHz and antiresonance at 1.51 GHz, ACBP channel displayed the maximum resonance at 1.19 GHz and

Table 1. Structural parameters of CdSe films coated onto glass and Al/Al_2O_3.

Samples	2θ max	I (a.u.)	D (nm)	$\in$ x 10^{-3}	SF%	δ (x10^{11} lines/cm^2)
Glass/*p*-CdSe	25.75	3972	26	6.28	0.30	5.26
Al/*n*-Al_2O_3/*p*-CdSe	25.85	4346	32	5.08	0.25	3.46
Al/*n*-Al_2O_3/*p*-CdSe/*n*-Bi_2O_3	25.75	2835	25	6.41	0.31	6.34

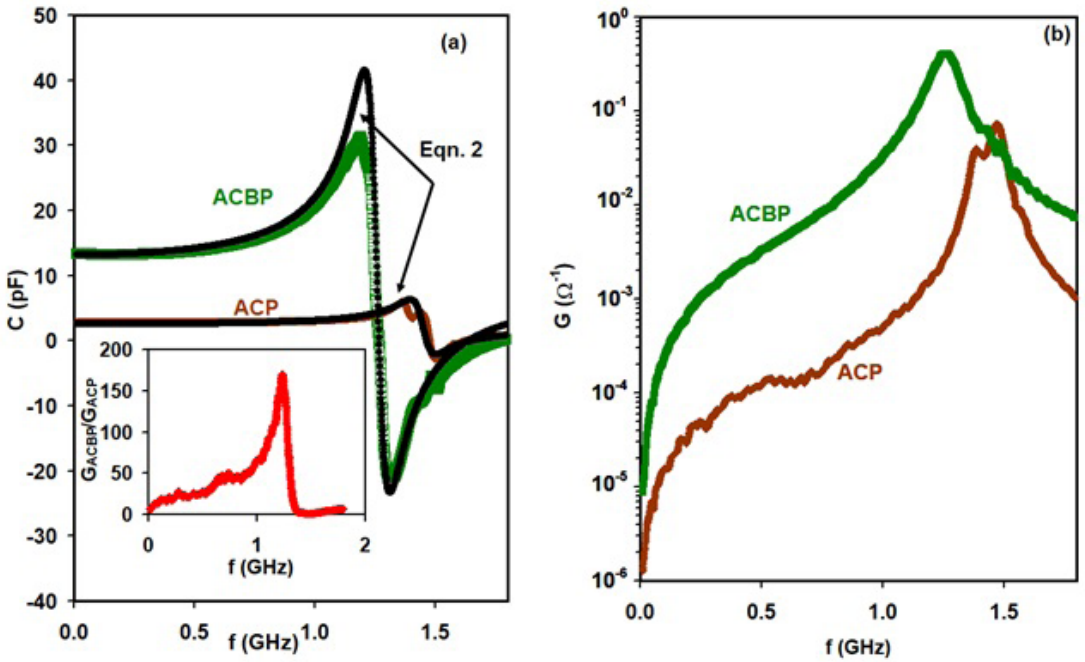

Figure 3. (a) the capacitance and (b) the conductance spectra for ACBP and ACP channels. Inset of (a) showing the ratio of the conductance of ACBP channel to that of ACP channel.

antiresonance at 1.33 GHz. The presence of oxide layer shifted the resonance and antiresonance critical frequencies to lower frequency values. It is also noted that the difference between maximum positive capacitance and negative capacitance at RA positions is much larger for ACBP channel than that of ACP channel. In other words, the presence of bismuth oxide nanosheets enhanced the negativity of the device capacitance making it more adequate as NC effect devices. RA and NC effects in electronic devices plays important role in canceling parasitic capacitance effect and reducing the noise in circuits. NC effect is also used to reduce the effective voltage drop across the gate dielectric in low power devices and ion sensitive field effect transistors[36,37]. NC effect reduces the power dissipation in electronic devices. In addition RA effect can be employed for the fabrication of permittivity sensors[38]. One of the possible reasons for NC effect is the traps presented in the crystallite boundaries[39]. Minority carrier injection could also account for this phenomena[40].

However to explore the role of Bi_2O_3 on the experimentally observed RA and NC effects, the relation between the geometrical capacitance or high frequency dielectric constant (ε_∞) and the dynamic part of the dielectric constant. The RA and NC phenomena can be described by Drude-Lorentz approach for dielectric dispersion in which[41],

$$C = \varepsilon_r(\omega)A/d = \left(\varepsilon_\infty + \frac{ne^2}{\varepsilon_o m^*}\frac{\omega_o^2-\omega^2}{\left(\omega_o^2-\omega^2\right)^2+(\gamma\omega)^2}\right)(A/d) = C_\infty + C_o - C_1 \quad (2)$$

Here, $C_\infty = \frac{A\varepsilon_\infty}{d}$, $C_o = \frac{A}{d}\frac{ne^2}{\varepsilon_o m^*}\frac{\omega_o^2}{\left(\omega_o^2-\omega^2\right)^2+(\gamma\omega)^2}$. , $C_1 = \frac{A}{d}\frac{ne^2}{\varepsilon_o m^*}\frac{\omega^2}{\left(\omega_o^2-\omega^2\right)^2+(\gamma\omega)^2}$, ω_o is to the effective oscillator frequency and $\gamma = \tau^{-1}$ is coefficient of electronic friction and known as the inverse of the scattering time constant (τ) of charge carriers. n and m^* are the number density of oscillators and the reduced effective mass of the ACBP dielectric layer, respectively. $m^* = \left[\frac{1}{m^*_{n-\,Al2O3}} + \frac{1}{m^*_{h-\,CdSe}} + \frac{1}{m^*_{n-\,BiO3}}\right]^{-1} = \left[\frac{1}{0.33m_o} + \frac{1}{0.102m_0} + \frac{1}{0.68m_o}\right]^{-1} = 0.07m_o$ [41-43]. For ACP layer the effective mass is $m^* = 0.09m_o$.

Equation 2 indicate that under conditions where C_1 is larger than $C_\infty + C_o$, the capacitance go negative. This condition is satisfied if $\gg \omega_o$. In fact, the fitting of the capacitance spectra which are shown by black colored circles in Figure 3a in accordance with Equation 2 was possible by substituting the values listed in Table 2. In accordance with the tabulated data, with the addition of Bi_2O_3 oxide layer the high frequency capacitance and the oscillator number increased whilst the oscillator frequency decreased and the scattering time constant remained constant. The enhanced dielectric constant or high frequency capacitance values that resulted from the coating of Bi_2O_3 layer is ascribed to the high polarization given by the accumulation of charge carriers at the additional interfaces (CdSe/Bi_2O_3)[44]. In addition, because ω_o is shifted from 1.45 GHz to 1.26 GHz, the difference between ω_o and ω become more pronounced leading to the enhanced NC effect in the ACBP channels.

Figure 3b show the conductance spectra for the device channels. Although both of the channels showed the same trend of variation which is presented by a conductance increase with increasing signal frequency reaching a maxima at 1.48 GHz and 1.26 GHz for ACP and ACBP channels, respectively. For all respective f values larger than 1.48 GHz and 1.26 GHz, the conductance decreases with increasing f. The role of Bi_2O_3 nanosheets on enhancing the conductance of the device is evident from the inset of Figure 3a. The inset illustrates the ratio of the conductance of the ACBP channel to the ACP channel. It is clear that the conductance has increased by more than 20 times at low frequencies and enhanced more and more reaching a value of 167 times at 1.26 GHz. The conductance is improved because of the incorporation of more oxygen[45] within CdSe structure because the ionic radius of O^{-2} being 138 pm[22] is much less than that of Se^{-2} (198 pm)[40].

Table 2. The parameters of the capacitance spectra for ACBP and ACP channels.

	ACP channel	ACBP channel
C_∞ (nF)	0.55	2.2
ω_o (GHz)	1.45	1.26
n (x10^{10} cm^{-3})	1.60	8.5
τ (ns)	1.50	1.5

3.4. High frequency antennas

To explore the ability of the ACP and ACBP channels to perform as a network antennas suitable for 5G/6G communications, the channel contact points and bars were sequentially imposed between the terminals of a network analyzer generating signals in the frequency domain of 0.009-6.0 GHz. The experimental setup for one port measurement is shown as inset-1 in Figure 4a. The reference signal of the setup before insertion of the device under test was always kept near zero dB. The measured reflection (S_{11}) and transition (S_{12}) coefficient parameters are shown in Figures 4a-d. Figure 4a illustrates the reflection coefficient parameter recorded from two point contacts (disk shaped antenna) each of area of 0.0314 cm^2. For this type of antennas the signal collected from ACP channel displayed values larger than -10 dBs. At 1.05 GHz, at 1.47 GHz and in the range of 2.49-4.11 GHz it showed S_{11} values of -13.3 dB, -17.2 dB and ~17.2 dB, respectively. ACBP channels disabled $S_{11} > -10\,\text{dB}$ at the same frequencies with very close S_{11} values. However, a sharp reflection peak of $S_{11} = -46\,\text{dB}$ appeared at carrier frequency of 3.10 GHz. The absence of this peak from the spectra of the ACP channel indicates that the deposition of Bi_2O_3 nanosheets onto CdSe dielectric layer remarkably improved their signal collection characteristics. Converting the values of the reflection coefficient to a linear scale benefiting from the equation[16],

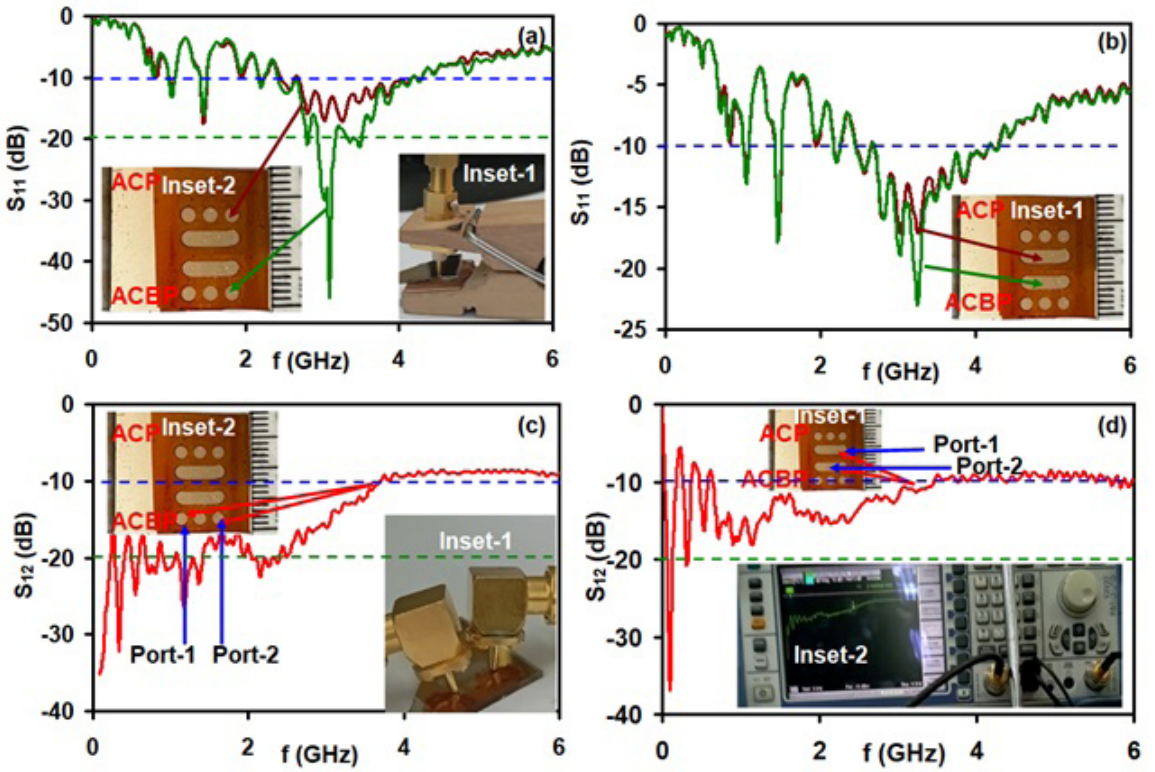

Figure 4. The reflection coefficients for (a) disk shaped antennas, (b) bar shaped antennas and the transmission spectra for two port (c) disk shaped antennas and (d) bar shaped antennas of ACP and ACBP channels. Inset-2, inset-1, inset-2 and inset-1 of (a), (b), (c), and (d), respectively, shows the measured contacts. Inset-1 of (a) and (c) showing the measuring probes for one-port two port antennas, respectively. Inset-2 of (d) showing an optical image for one of the collected signals.

Table 3. List of different antenna designs used in 5G/6G technology networks.

Antenna Type	Frequency Band (GHz)	S11 (dB)	Additional functionality	Reference
$SrBi_2Nb_2O_9$ dielectric Antenna	2-4 (4G/5G)	< -10	---	Abreu et al.[46]
Rectangular Microstrip Antenna Array	27.5 (5G)	< -30		Didi et al.[47]
Cylindrical dielectric resonator	27-34 (5G/6G)	< -31	RA	Dutta et al.[48]
Quasi-Yagi antenna	27-30 (5G/6G)	< -10		Lak[49]
Low Noise Amplifier	1-11	<-10	NC, amplifier	Liu et al.[50]
ASBP antenna	20 (5G/6G)	<-6	*MOS	Alawneh et al.[16]
ACBP	5G/6G	<-46	NC, RA	Current work

*MOS: Metal-oxide-semiconductor capacitors, RA: resonance antiresonance, NC negative capacitance.

$$|\Gamma|^2 = \left(10^{dB/20}\right)^2 \quad (3)$$

It is possible to determine the magnitude of power reflection (Ã). Ã showed values of for ACP and ACBP channels 0.136 and 5.0×10^{-3}, respectively. An enhancement of the power reflection by more than three orders of magnitude is achieved via Bi_2O_3 coating. The numerical data here predicted a power rejection of 13.6% and transmission of 86.4% is achieved at 3.10 GHz. Coating of the bismuth oxide as a second oxide layer decreased the reflection to 0.50% and increased the transmission to 99.5%. A highly efficient antenna for the ACBP channel.

Figure 4b show the output (S_{11}) achieved from bar shaped antennas. Bar shaped ACP channels as antennas exhibited S_{11} values of -12.6 dB, -17.7 dB and -13.7 dB at carrier frequency of 1.05 GHz, 1.44 GHz and in the range of 2.49-4.11 GHz, respectively. Once again Bi_2O_3 nanosheets enhanced the performance of the antennas allowing signal rejection of 7.1% and transmission of 92.9% at 3.24 GHz. ACBP channels are more efficient as 5G/6G antennas than ACP channels. For channels of similar characteristics disk shaped antennas are more efficient that bar shaped antennas.

Figures 4c and 4d illustrate the power transmission parameters obtained for two port antennas. Here S_{12} determines the reverse transmission power from port-2 (output) to port-1 (input). This type of measurement provides information about the level of output power that can pass from one port to another. The idea here is to treat the antennas as network antennas. Figure 4c show S_{12} parameter collected on ACBP channel between two disk shaped antennas 4.0 mm apart. The experiment is displayed as inset-1 in Figure 4c. It is clear from the figure that efficient power transmission exceeding -20 dBs is possible for all carrier frequencies in the range of 0.009-2.46 GHz. The linear $S_{12} = 10^{S_{12}(dB)/20}$ parameter cannot exceed 10% in that range whilst 36.3% pass from one port to another in the range of 3.75-6.0 GHz.

Figure 4d show the transmission parameter for bar shaped antennas one located on ACP and the other on ACBP channel. The optical image shown as inset-2 in the figure shows one of the collected signals. The two bars antennas are also shown in inset-1 of the same figure. For this network transmission signal remains below -20 dB in all the studied range except for a narrow peak detected at 90 MHz. For most of the carrier frequencies S_{12} parameter fluctuates between -10 dB and -20 dB. Indicating that the signal transmission from one port to another when they are 2.0 mm apart varies in the range of 10%-36.3%. For carrier of frequency of 90 MHz, S_{12} parameter reaches -36.9 dB. The transmission here can be as low as 1.4%. The numerical data for S_{12} parameter indicate that even the disk shaped or bar shaped antennas is located on the same surface close to each other coupling between them is hardly possible and the ACBP devices can be used for the fabrication of 5G/6G antenna arrays.

It is interesting to compare the currency developed ACBP design with that of Ag/*n*-Si/*n*-Bi_2O_3/Pt (ASBP) quad band antennas[16]. These devices were also nominated for 5G/6G technology applications. ASBP devices exhibited S_{11} and S_{22} parameters of values of -6 dB and -7 dB, respectively. The isolation between the two ports of this antenna reached 28 dB[16]. ACBP devices showed more enhanced characteristics compared to ASBP devices. For examples, *S*11 parameter reached –46 dB at carrier frequency of 3.10 GHz. Signal transmission efficiency reached 99.5% at this frequency. Although the disk or bar shaped antennas are only 2.0 mm or 4.0 mm apart, the interference between the ports is weak indicating the possibility of using the ACBP antennas as arrays. These arrays are always employed for applications where enhanced signal strength, directivity, and interference mitigation are needed. Further comparison with other devices are listed in Table 3.

4. Conclusions

The study demonstrates that CdSe thin films deposited on Al/Al_2O_3 substrates and partially recoated with Bi_2O_3 nanosheets exhibit multifunctional electronic properties. The well-aligned conduction bands and valence band offsets enhance charge transport, while structural investigations confirm improved crystallinity. The ACP and ACBP channels exhibit notable resonance-antiresonance (RA) and negative capacitance (NC) effects, with Bi_2O_3 nanosheets significantly amplifying these properties. Additionally, ACBP channels show substantial conductance enhancement and superior microwave antenna performance, with improved power reflection and transmission characteristics. These findings highlight the potential of ACBP channels for advanced electronic applications, particularly in high-frequency communication systems such as 5G/6G technologies.

5. Acknowledgments

This work was funded by the deanship of scientific research at Arab American University (AAUP), Jenin, Palestine and by Istinye University. The authors therefore acknowledge the financial support of the AAUP and Istinye University. The authors would also acknowledge and thank Dr. Isam Alawneh and Dr. Tarek Zannon for their support in evaluating and measuring the antenna parameters.

6. References

1. Baruah S, Borah J, Maity S, Rajasekaran S. Analytical investigation of CdSe/CdS/ZnSe-based single-core double-shell nanotextured vertical nanopillar array antenna for broadband photodetection applications. Int J Commun Syst. 2024;37(8):e5752.
2. Shi J, Yoo D, Vidal-Codina F, Baik CW, Cho KS, Nguyen NC, et al. A room-temperature polarization-sensitive CMOS terahertz camera based on quantum-dot-enhanced terahertz-to-visible photon upconversion. Nat Nanotechnol. 2022;17(12):1288-93.
3. Bahk YM, Kim KH, Ahn KJ, Park HR. Recent developments in terahertz nanosensors. Advanced Photonics Research. 2024;5(1):2300211.
4. Chavan GT, Sikora A, Chaure NB, Deshmukh LP, Jeon CW. A novel highly conductive chalcogenide material: Cd1-xAlxSe thin films. Mater Lett. 2022;320:132353.
5. Nahar T, Rawat S. Efficiency enhancement techniques of microwave and millimeter-wave antennas for 5G communication: a survey. Trans Emerg Telecommun Technol. 2022;33(9):e4530.
6. Bai Z, Hao L, Zhang Z, Huang Z, Qin S. Enhanced photoluminescence of corrugated Al2O3 film assisted by colloidal CdSe quantum dots. Nanotechnology. 2017;28(20):205206.
7. Freeman EC, Luo FC. Traps at the Al2O3/CdSe interface. J Appl Phys. 1982;53(7):5294-303.
8. Dai M, Sun G, Yu H, Wang S, Niyato D. User association and channel allocation in 5G mobile asymmetric multi-band heterogeneous networks. IEEE Trans Mobile Comput. 2024;24(4):3092-109.
9. Hongyun C, Mengyao Y, Xue P, Ge X. Joint active and passive beamforming design for hybrid RIS-Aided integrated sensing and communication. China Commun. 2024;21(10):1-12.
10. Zhang Y, Gang Y, Wu P, Fan G, Xu W, Ai B, et al. Integrated sensing, communication, and computation in sagin: joint beamforming and resource allocation. IEEE Trans Cogn Commun Netw. 2025;11(5):3128-43.
11. Li P, Li R, Fan Z, Han J, Ding G, Wang Q, et al. 3D printed high-temperature ceramic conformal array antenna: Design, analysis, manufacturing, and testing. Defence Technol. 2025. In press.
12. Wang Q, Li P, Zhang Y, Tan G, Yang Y, Rocca P. Robust design and tolerance analysis of shaped reflector antennas based on interval analysis. IEEE Antennas Wirel Propag Lett. 2025;24(8):2392-6.
13. Giri SK. Effect of Sintering Additives (V2O5, B2O3, Bi2O3) on the Electrical Properties of substituted Y-type Hexagonal Ferrite, Ba2Co0. 6Cu0. 4Zn1. 0Fe12O22 [dissertation]. Rourkela: National Institute of Technology; 2016.
14. Liew XT, Chan KC, Kong LB. Magnetodielectric Ni ferrite ceramics with Bi2O3 additive for potential antenna miniaturizations. J Mater Res. 2009;24(2):324-32.
15. Majid A, Bibi M. Cadmium based II-VI semiconducting nanomaterials. Gewerbestrasse. 2018;11:6330.
16. Alawneh I, Qasrawi AF, Zanoon T, Khanfar HK. Isotype n-Si/n-Bi2O3 heterojunctions designed as high-frequency MOS devices, microwave band filters and quad band 5G/6G antennas. J Electron Mater. 2025;54(5):4175-85.
17. Mishra N, Rathore D, Pandey RK. A comparative study of conventional type II and inverted core–shell nanostructures based on CdSe and ZnS. Opt Quantum Electron. 2018;50(2):107.
18. Al-Kotb MS, Al-Waheidi JZ, Kotkata MF. Opto-electronic characterizations of oriented nano-structure CdSe film/Si (0 0 1) heterostructure. Superlattices Microstruct. 2014;69:149-63.
19. Khusayfan NM, Qasrawi AF, Khanfar HK. Impact of Yb, In, Ag and Au thin film substrates on the crystalline nature, Schottky barrier formation and microwave trapping properties of Bi2O3 films. Mater Sci Semicond Process. 2017;64:63-70.
20. Liang T, Guo X, Guan B, Guo J, Gu X, Lin Q, et al. Current-voltage characteristics of p-GaAs/ n-GaN heterojunction fabricated by wafer bonding. Appl Phys Lett. 2007;90(10):102107.
21. Maity SK, Pandit S. Study of analog and RF performance of UTB-OI-Si substrate MOS transistor using buffered InGaAs and Silicon channel. In: 2015 6th International Conference on Computers and Devices for Communication (CODEC); 2015 Dec 16-18; Kolkata, India. Proceedings. New York: IEEE; 2015. p. 1-4.
22. Qasrawi A, Khanfar H. Effect of Ag 2 O nanosheets thickness on the performance of Al/GeO 2/Ag 2 O/GeO 2/C multifunctional electronic devices. Journal of the Arab American University. 2023;9(1)
23. Pedro AA, Arlievskii MP. Monitoring the composition of normal electrocorundum melt by means of the constant phase voltage. Steel Transl. 2012;42(8):646.
24. Qasrawi AF. Formation and negative capacitance effect in Au/Bi2o3/Zns/Ag heterojunctions designed as microwave resonators. Chalcogenide Lett. 2018;15(12):605-13.
25. Akshaykranth A, Ajayan J, Bhattacharya S, Mounika B. Exploration on the impact of barrier thickness, gate recess, and lateral scaling on AlGaN/GaN SRL HEMT on silicon for future RF power electronics. J Mater Sci Mater Electron. 2024;35(15):1006.
26. Mohiddon MA, Krishna MG, Dalba G, Rocca F. Transmission electron microscopy study of Ni–Si nanocomposite films. Mater Sci Eng B. 2012;177(13):1108-12.
27. Kumar KDA, Mele P, Anitha M, Varadharajaperumal S, Alagarasan D, Alhokbany NS, et al. Simplified chemical processed Cd1− x Al x S thin films for high-performance photodetector applications. J Phys Condens Matter. 2021;33(19):195901.
28. Alharbi SR, Algarni SE. Growth and characterization of (glass, Ag)/SeO2 thin films. Physica B. 2022;633:413790.
29. Qasrawi AF, Toubasi AJ. Iron selenide nanowire bundles for microwave communication technology. Phys Status Solidi. 2024;221(3):2300450.
30. Khusayfan NM, Khanfar HK. Formation mechanism, structural and optoelectronic properties of As2Se3/CdS heterojunctions prepared by physical vapor deposition technique. J Electron Mater. 2019;48(7):4368-74.
31. Verma KC, Goyal N, Kotnala RK. Lattice defect-formulated ferromagnetism and UV photo-response in pure and Nd, Sm substituted ZnO thin films. Phys Chem Chem Phys. 2019;21(23):12540-54.
32. Agafonov D, Bobyl A, Kamzin A, Nashchekin A, Ershenko E, Ushakov A, et al. Phase-homogeneous LiFePO4 powders with crystallites protected by ferric-graphite-graphene composite. Energies. 2023;16(3):1551.
33. Ghosh OSN, Gayathri S, Allam SR, Sharan A, Lal SS, Reddy MJK, et al. Bound exciton engineering approach for tuning the thermal lensing phenomenon in anatase TiO2: gd nanosystems. Chemical Physics Impact. 2024;9:100679.
34. Anwar MS, Bangert A. Broadband antenna simulation and practical challenges - factors influencing poor mismatch between simulated and measured results. In: 2019 International Workshop on Antenna Technology (iWAT); 2019 Mar 3-6; Miami. Proceedings. New York: IEEE; 2019. p. 33-36.
35. Pozar DM. Microwave engineering: theory and techniques. Hoboken: John Wiley & Sons; 2021.
36. Sanjay S, Sakib FI, Hossain M, Bhat N. Super-Nernstian WSe 2/ MoS 2 heterostructure ISFET combining negative capacitance and charge screening effects. IEEE Sens J. 2023;23(12):12526-35.

37. Naidu ML, Patnaik MV, Sinha SK, Chander S, Chaudhary R. NCTFET device for low power VLSI application. In: 2023 International Conference on Sustainable Computing and Smart Systems (ICSCSS); 2023 Jun 14-16; Coimbatore, India. Proceedings. New York: IEEE; 2023. p. 1127-1132.
38. Canalias X, Casacuberta P, Vélez P, Su L, Martín F. Highly sensitive transmission-mode phase-variation permittivity sensor based on resonance and antiresonance. IEEE Trans Microw Theory Tech. 2024;73(3):1619-31.
39. Fernandes JD, Vieira DH, Klem M, Alves N. Dinaphtho [2, 3-b: 2′, 3′-f] thieno [3, 2-b] thiophene photoresistor: Generation of photocarriers and charge trapping. Mater Sci Semicond Process. 2023;165:107621.
40. Alfhaid LHK, Qasrawi AF. Characterization and applications of ITO/SeO2 interfaces. Opt Quantum Electron. 2022;54(7):423.
41. Qasrawi AF. Optically controlled n− Si/p− SeO2/p− SiO2 microwave resonators designed for 5G/6G communication technology. Phys Scr. 2023;98(9):095925.
42. Chitrada KC, Raja KS, Gakhar R, Chidambaram D. Enhanced photoelectrochemical performance of anodic nanoporous β-Bi2O3. J Electrochem Soc. 2015;162(6):380.
43. Pu T, Shen H, Tang Q. Simulation of a charged Al2O3 film as an assisting passivation layer for a-Si passivated contact P-type silicon solar cells. Silicon. 2022;14(7):3339-48.
44. Chisca S, Musteata VE, Sava I, Bruma M. Dielectric behavior of some aromatic polyimide films. Eur Polym J. 2011;47(5):1186-97.
45. Maman N, Templeman T, Manis-Levi H, Shandalov M, Ezersky V, Sarusi G, et al. Postgrowth control of the interfacial oxide thickness in semiconductor–insulator–semiconductor heterojunctions. Adv Mater Interfaces. 2018;5(12):1800231.
46. Abreu RF, Silva FR, Saturno SO, Colares DDM, Abreu TO, Nascimento JPC, et al. Effects of La2o3 and Bi2O3 additions on the microwave dielectric and antenna properties of Srbi2nb2o9 ceramic matrix. Journal of Mechatronics Engineering. 2022;4(2):2-11.
47. Didi S, Halkhams I, Fattah M, Balboul Y, Mazer S, El Bekkali M. Study and design of printed rectangular microstrip antenna arrays at an operating frequency of 27.5 GHz for 5G applications. Journal of Nano and Electronic Physics. 2021;13(6):06035.
48. Dutta D, Shanmuganantham T, Sahu S. Wideband Cylindrical Dielectric Resonator Antenna with Defected Ground for 5G, 6G, and mmWave Application. In: 2024 IEEE Pune Section International Conference (PuneCon); 2025 Dec 12-15; Pune, India. Proceedings. New York: IEEE; 2024. p. 1-5.
49. Lak A. Parameter study of a 5G array antenna at 28 GHz. Sci Rep. 2025;15(1):1948.
50. Liu Z, Boon CC, Yu X, Li C, Yang K, Liang Y. A 0.061-mm^2 1–11-GHz noise-canceling low-noise amplifier employing active feedforward with simultaneous current and noise reduction. IEEE Trans Microw Theory Tech. 2021;69(6):3093-106.

Data Availability

The data that support the findings of this study are available from the corresponding author upon reasonable request.